SOLAR CELLS

Stabilizing heterostructures of soft perovskite semiconductors

Yanbo Wang[1], Tianhao Wu[1], Julien Barbaud[1], Weiyu Kong[1], Danyu Cui[1], Han Chen[1], Xudong Yang[1,2]*, Liyuan Han[1,2,3]*

Here we report a solution-processing strategy to stabilize the perovskite-based heterostructure. Strong Pb–Cl and Pb–O bonds formed between a $[CH(NH_2)_2]_x[CH_3NH_3]_{1-x}Pb_{1+y}I_3$ film with a Pb-rich surface and a chlorinated graphene oxide layer. The constructed heterostructure can selectively extract photogenerated charge carriers and impede the loss of decomposed components from soft perovskites, thereby reducing damage to the organic charge-transporting semiconductors. Perovskite solar cells with an aperture area of 1.02 square centimeters maintained 90% of their initial efficiency of 21% after operation at the maximum power point under AM1.5G solar light (100 milliwatts per square centimeter) at 60°C for 1000 hours. The stabilized output efficiency of the aged device was further certified by an accredited test center.

The performance of perovskite solar cells (PSCs) relies on generation and extraction of charge carriers in working devices (*1*–*6*). Generally, it is the semiconductor heterostructure formed by perovskites and organic or inorganic electron-transporting layers (ETLs) and hole-transporting layers (HTLs) that enables photogenerated charge-carrier extraction. Construction of defect-free heterostructures is critical for large-scale application of perovskite-based optoelectronic devices (*7*–*9*). On the perovskite side of the heterostructure, component elements are assembled by relatively weak chemical bonds, including ionic bonds, hydrogen bonds, and van der Waals interactions (*10*–*12*). Because of their weak bonding nature, the soft crystal lattice of perovskites is easily decomposed, normally starting at the surface, and leads to great difficulties in forming stable heterostructures on perovskite surfaces. Several reports have demonstrated that perovskite components can permeate through the ETLs and HTLs, disordering the favored heterostructure and decreasing the charge extraction (*13*, *14*). Degradation of the heterostructure is accelerated by multiple factors such as illumination, heat, and electric fields (*15*–*17*).

Here we report a solution-processing strategy to stabilize the perovskite heterostructure by forming strong chemical bonds at the surface of soft perovskite films that can largely impede the loss of perovskite components, resulting in less damage to the organic HTL. In addition, the band offset of the heterostructure can benefit the hole extraction between the perovskite and the HTLs. We fabricated PSCs with efficiencies approaching 21% on an aperture area of 1.02 cm^2. The PSC with stabilized heterostructure exhibited excellent operational stability, maintaining 90% of its initial value after aging under operation conditions of AM1.5G solar light, 100 mW cm^{-2} at the maximum power point, under 60°C for 1000 hours. We also sent the aged device to a public test center [Calibration, Standards and Measurement Team at the Research Center for Photovoltaics, National Institute of Advanced Industrial Science and Technology (AIST), Japan]; a certified stabilized efficiency of 18.6% was obtained, still maintaining ~90% of its initial value.

The heterostructure consists of (i) a perovskite film with a surface rich in Pb and (ii) a chlorinated graphene oxide (Cl-GO) layer, where strong Pb–Cl and Pb–O bonds are formed to join the two layers. Figure 1A illustrates the formation of the Pb surface–rich perovskite film of $[CH(NH_2)_2]_x[CH_3NH_3]_{1-x}Pb_{1+y}I_3$ (also noted as $FA_xMA_{1-x}Pb_{1+y}I_3$). We used a dilute $Pb(SCN)_2$ solution as the Pb source that was spin-coated onto the perovskite film surface. The perovskite film with a surface rich in Pb was formed by heat treatment to remove volatile organic components like FASCN (formamidinium thiocyanate) or MASCN (methylamine thiocyanate).

We probed the surface of the perovskite film by x-ray photoelectron spectroscopy (XPS) (Fig. 1B). The peak intensity of Pb 4f core levels increased when more $Pb(SCN)_2$ was spin-coated onto the perovskite surface, whereas the peak intensity of I 3d core levels decreased (Fig. 1C), indicating the fabrication of a perovskite layer with a surface rich in Pb. The top morphology of the perovskite layer was not changed, as determined by scanning electron microscopy (Fig. 1D and fig. S1, A to E). The roughness of the Pb surface–rich perovskite layer was 25.1 ± 2.1 nm (Fig. 1E). The corresponding surface potential mapping and phase image are shown in fig. S2, A and B. Notably, $Pb(COOH)_2$ had an effect similar to $Pb(SCN)_2$, forming Pb surface–rich perovskite layers.

To form a stable heterostructure on the perovskite layer, we constructed strong chemical bonds of Pb–O and Pb–Cl by deposition of Cl-GO. A C-Cl peak at the binding energy of 289 eV appeared in the x-ray photoelectron spectrum of the C 1s core level in Cl-GO, in contrast to the x-ray photoelectron spectrum of GO (fig. S3, A and B) (*18*). We used scanning electron microscopy (SEM) to observe the perovskite/Cl-GO layer in comparison with the perovskite/GO layer. The surface of the perovskite/GO film was rough with poor uniformity (Fig. 2A), but Cl-GO spread well on the surface of perovskite film (Fig. 2B). Atomic force microscopy (AFM) over a large area (25 μm by 25 μm) on the film surface (Fig. 2, C and D) revealed surface roughnesses of 62.6 ± 24.31 nm and 24.6 ± 2.37 nm for perovskite/GO and perovskite/Cl-GO, respectively.

We also conducted Kelvin probe force microscopy (KPFM) to compare the work functions (WFs) of the corresponding three samples (figs. S2A and S4, A and B) (*19*). The surface potential distribution of perovskite/GO was relatively nonuniform compared with the potential distribution of the other two samples. After the calibration of the surface potential of the tip with Au reference (ψ_{Au}=5.10 eV), the WFs of each sample were 5.36, 5.33, and 5.43 eV, for perovskite, perovskite/GO, and perovskite/Cl-GO, respectively. The small difference in WFs between the perovskite and perovskite/GO samples was likely the result of the poor coverage or contact of GO that would not obviously change the WFs of perovskite. However, the WF of perovskite/Cl-GO was much different from that of perovskite and was near the Fermi level (E_F) of Cl-GO measured by ultraviolet photoelectron spectroscopy (UPS) (fig. S5, A and B) (*20*), indicating that Cl-GO made uniform contact with the surface of perovskite with high coverage.

We measured the x-ray photoelectron spectra of perovskite, perovskite/GO, and perovskite/Cl-GO to evaluate whether the good contact and coverage of perovskite/Cl-GO was the result of strong chemical bonding. No obvious change in the Pb 4f core level was observed between perovskite and perovskite/GO (Fig. 2E) (*21*), and we attributed this result to the poor coverage or contact of GO. However, the Pb 4f core level shifted up by 0.3 eV for perovskite/Cl-GO. We analyzed the O 1s core levels in x-ray photoelectron spectra for the pure GO, Cl-GO, perovskite/GO, and perovskite/Cl-GO (Fig. 2F). The O 1s core level of Cl-GO shifted from 532.21 to 532.52 eV, which indicates that O in Cl-GO would have stronger electron-withdrawing properties. In addition, the O 1s binding energy of perovskite/Cl-GO is ~0.10 eV lower than that of perovskite/GO, indicating that the oxidation state of O in Cl-GO is even lower than that in GO. These XPS results indicate that the Pb–O bond within perovskite/Cl-GO is stronger than that of perovskite/GO. In addition, we also observed the Cl 2p core levels of Cl-GO at 198.85 and 200.30 eV shift to 197.85 and 199.40 eV in perovskite/Cl-GO, respectively (Fig. 2G), indicating the formation of Pb–Cl bonds (*22*).

We used density functional theory (DFT) to calculate the electron density profiles of O in GO

[1]State Key Laboratory of Metal Matrix Composites, Shanghai Jiao Tong University, Shanghai 200240, China. [2]Center of Hydrogen Science, School of Materials Science and Engineering, Shanghai Jiao Tong University, Shanghai 200240, China. [3]Photovoltaic Materials Group, Center for Green Research on Energy and Environmental Materials, National Institute for Materials Science, Tsukuba, Ibaraki 305-0047, Japan.
*Corresponding author. Email: yang.xudong@sjtu.edu.cn (X.Y.); han.liyuan@sjtu.edu.cn (L.H.)

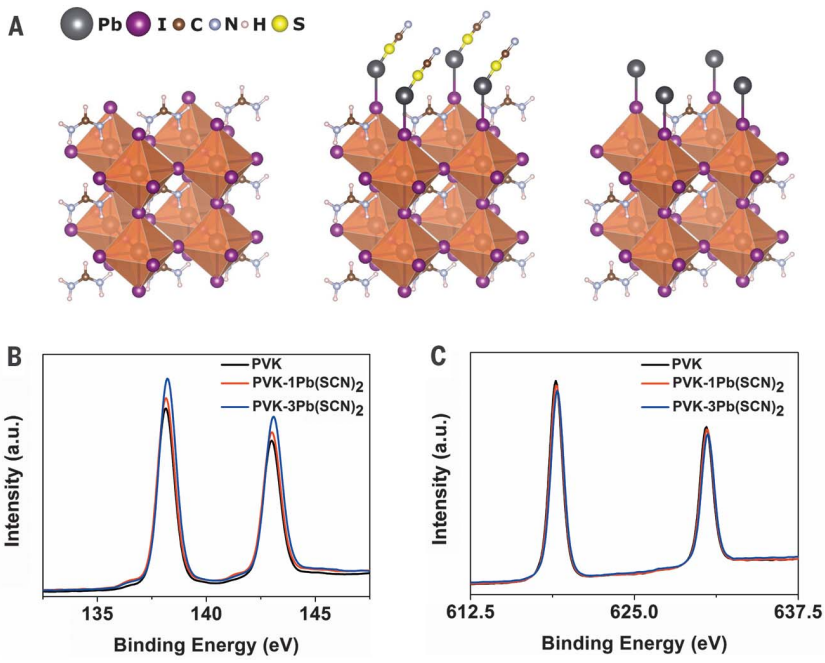

Fig. 1. Schematic of the fabrication process of the Pb surface–rich perovskite layer and characterization by XPS, SEM, and AFM. (**A**) Schematic drawing of the conversion process from the pristine perovskite layer, the layer treated with $Pb(SCN)_2$, and the Pb surface–rich perovskite layer. (**B**) XPS results of Pb 4f core levels of the pristine perovskite surface and the Pb surface–rich perovskite. PVK, perovskite; a.u., arbitrary units. (**C**) XPS results of I 3d core levels of the pristine perovskite surface and the Pb surface–rich perovskite. (**D** and **E**) (D) SEM image of the top morphology of the Pb surface–rich perovskite [Pb-1Pb$(SCN)_2$] and (E) *xy*-plane film morphology of the PVK-1Pb$(SCN)_2$ measured by AFM. PVK-1Pb$(SCN)_2$ and PVK-3Pb$(SCN)_2$ denote perovskite treated with 10 or 30 μl of a dilute solution of $Pb(SCN)_2$.

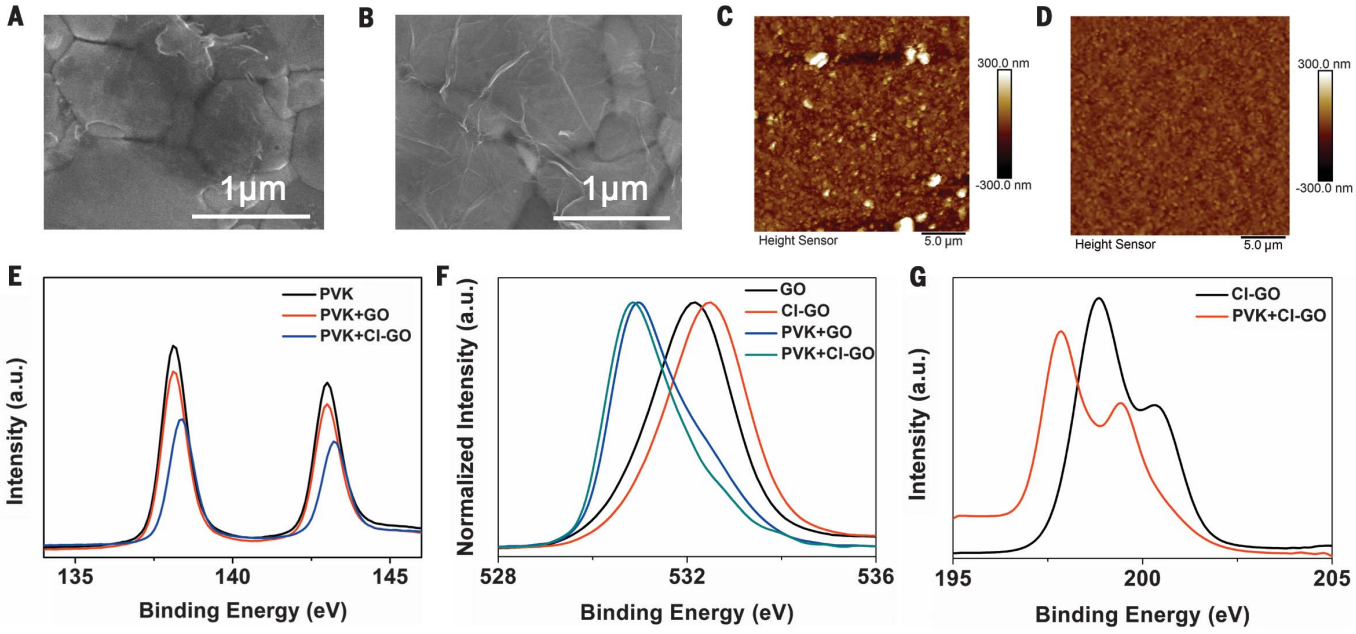

Fig. 2. Characterization of GO/Cl-GO on the surface of perovskite layer. (**A** and **B**) Top SEM image of (A) perovskite/GO and (B) perovskite/Cl-GO. (**C** and **D**) *xy*-plane film morphology of (C) perovskite/GO and (D) perovskite/Cl-GO measured by AFM. (**E**) X-ray photoelectron spectrum of the Pb 4f core level of the perovskite layer (black), perovskite/GO (red), and perovskite/Cl-GO (blue). (**F**) X-ray photoelectron spectrum of the O 1s core level of GO (black), Cl-GO (red), perovskite/GO (blue line), and perovskite/Cl-GO (green). (**G**) X-ray photoelectron spectrum of the Cl 2p core levels of Cl-GO (black) and perovskite/Cl-GO (red). For ease of comparison, the scale bars in (C) and (D) are the same as that in Fig. 1E.

(fig. S6A) and structurally optimized Cl-GO (fig. S6B). The Cl atom develops a bonding orbital with the closest carbon. We evaluated the influence of the chloride on the neighboring atoms by using projected density of states (PDOS) to verify the shift in O 1s. The PDOS of Cl-GO is the shifted image of GO, with a ~0.30-eV difference (fig. S7A). The matching of the shifted peaks (~0.31-eV shift) is shown in fig. S7B. This ~0.30-eV shift between the energies of electrons on the O 1s orbitals is in good agreement with the experimental value obtained by XPS and shows that DFT simulations confirm the influence of the Cl atom on the binding energy of the O 1s orbitals.

We further compared the energy levels of Cl-GO with other HTLs. The bandgap of Cl-GO was determined by ultraviolet-visible (UV-vis) absorption spectroscopy (fig. S8A) and calculated by the Kubelka-Munk function–converted plots (fig. S8B) (*23*). When combined with the UPS results (fig. S5), the energy levels of Cl-GO were obtained (fig. S9). The valence band maximum (VBM) of the perovskite was also measured by UPS to be −5.80 eV (fig. S10) (*24*). The highest occupied molecular orbital (HOMO) level of Cl-GO (−5.45 eV) is in the middle of the VBM of perovskite (−5.80 eV) and the HOMO level of polytriarylamines (PTAA) (−5.16 eV; fig. S11) or 2,2′,7,7′-tetrakis(*N*,*N*-di-*p*-methoxyphenylamine)-9,9′-spirobifluorene (Spiro-MeOTAD) (−5.10 eV; fig. S12), respectively (*25*, *26*), which would provide a more efficient pathway for the extraction of holes than GO (with a HOMO energy level of −5.85 eV).

To reveal the effect of perovskite/Cl-GO on the stability of heterostructure and the device, we measured the HOMO level of the HTL of a device with the structure of conducting glass/ETL/perovskite/HTL/Au electrode. The HTL was PTAA or Spiro-MeOTAD. The device was encapsulated and then aged at the maximum power point under light-soaking (AM1.5G, 100 mW cm^{-2}) for 200 hours at 60°C. We removed the package and Au electrode and measured the HTL of PTAA or Spiro-MeOTAD by UPS (figs. S11 and S12). From the high–binding energy region of the ultraviolet photoelectron spectra, we could see that the E_F of each material did not change appreciably, but the difference in the low–binding energy region indicates that the gap between the Fermi level and the HOMO energy level became larger. Thus, the aged PTAA and Spiro-MeOTAD were no longer typical p-type materials.

In contrast, we fabricated a device with a heterostructure of perovskite/Cl-GO/HTL, as well as a GO-based device as a reference. The fresh sample was first measured by AFM and KPFM to obtain the initial morphology and surface potential information (fig. S13). The corresponding devices with electrodes and encapsulation were aged with the same UPS aging test. After removing the package and Au electrode, we observed that the morphology of perovskite/PTAA and perovskite/GO/PTAA (fig. S14, A and B) differed substantially from that of the fresh perovskite/PTAA sample (fig. S13A). In contrast, the perovskite/Cl-GO/PTAA sample preserved the original morphology (fig. S14C), even though no appreciable difference in roughness was observed for all three samples. The surface potential of aged perovskite/Cl-GO/PTAA was consistent with that of the fresh sample, but the surface potential of the aged perovskite/PTAA and perovskite/GO/PTAA is 68 and 31 mV higher, respectively, than that of the fresh sample (Fig. 3, A to C). In addition, the surface potential distribution of the aged samples is analyzed in fig. S15; the aged sample with Cl-GO showed the narrowest distribution, indicating the homogeneous surface of PTAA in the perovskite/Cl-GO device. The same tendency was observed for the Spiro-MeOTAD–based samples (figs. S16 to S18). As a result, we can conclude that a stabilized heterostructure of perovskite/Cl-GO/HTL was formed.

We also analyzed the spatial distribution of perovskite components within Spiro-MeOTAD by time-of-flight secondary ion mass spectroscopy (TOF-SIMS) for the devices after the UPS aging test (fig. S19). The count of the I^- signal from the Spiro-MeOTAD layer is substantially reduced for perovskite/Cl-GO. The mapping signal of I^- in Spiro-MeOTAD was counted and presented by pixel ratio in Fig. 3, D to F. The HTL material layers in the aged control device and the perovskite/GO-based device were already fully occupied by I^-, whereas only a low signal was observed from the aged perovskite/Cl-GO sample.

We tested the thermal stability of the perovskite/Cl-GO heterostructure by aging the samples at 85°C for 150 hours under a nitrogen atmosphere.

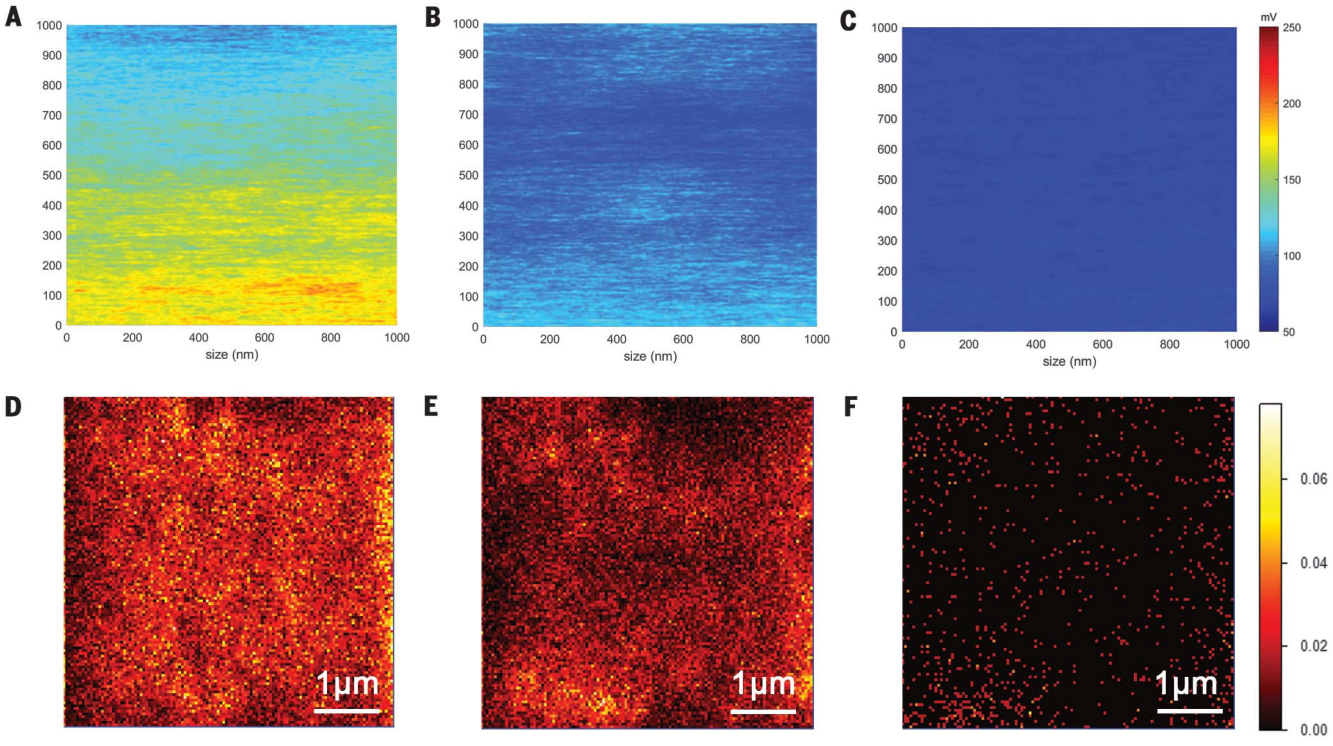

Fig. 3. Degradation of organic HLTs probed by KPFM and TOF-SIMS. (**A** to **C**) *xy*-plane potential mapping images of (A) perovskite/PTAA, (B) perovskite/GO/PTAA, and (C) perovskite/Cl-GO/PTAA measured by KPFM. (**D** to **F**) Mapping of TOF-SIMS signals of I^- in the HTLs for (D) perovskite/Spiro-MeOTAD, (E) perovskite/GO/Spiro-MeOTAD, and (F) perovskite/Cl-GO/Spiro-MeOTAD. All samples were aged after 200 hours of light-soaking at the maximum power point at 60°C.

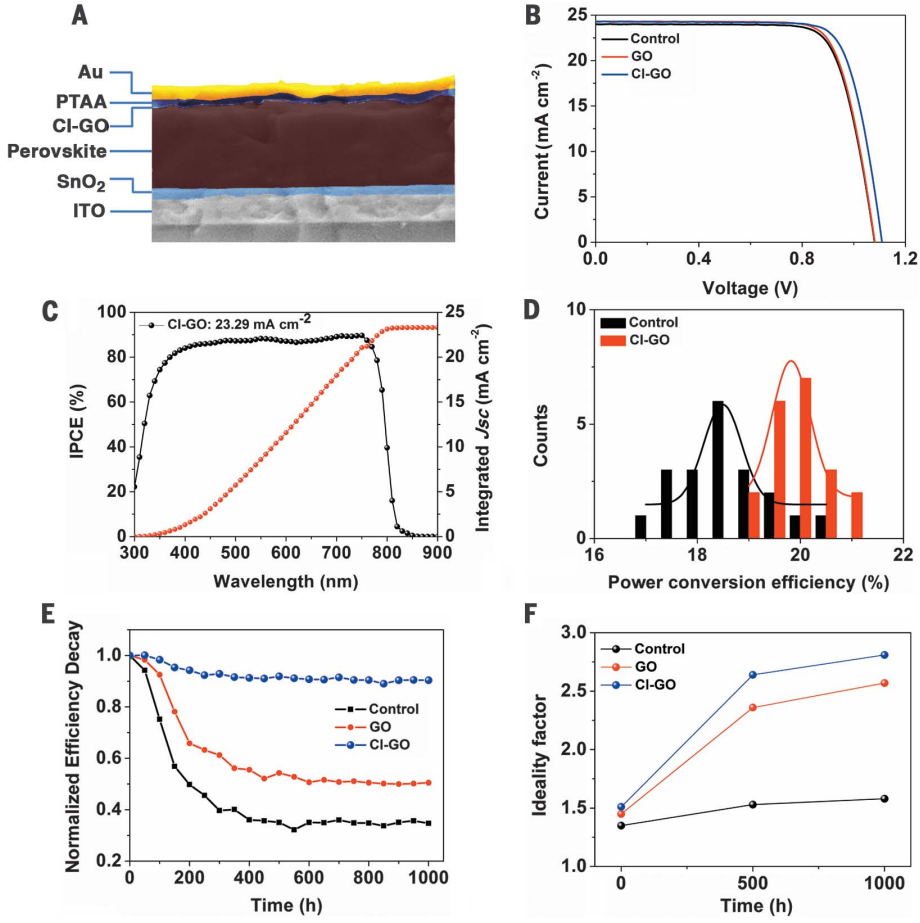

Fig. 4. Structure and performance of the PSC with an aperture area of 1.02 cm^2. (**A**) Cross-sectional SEM image of the cell. ITO, indium tin oxide. (**B**) *I-V* curves of the cells measured under forward scan. (**C**) IPCE spectrum and integrated current of the cell with perovskite/Cl-GO. *Jsc*, short-circuit current density. (**D**) Histogram of average power conversion efficiency values of the cell. (**E**) Operational stability of the control cell and the cell with GO or Cl-GO. (**F**) Ideality factors of the cells with perovskite/PTAA, perovskite/GO/PTAA, or perovskite/Cl-GO/PTAA before and after the aging test. The aging test was conducted under 1000 hours of light-soaking (AM1.5G, 100 mW cm^{-2}) at the maximum power point at 60°C. All cells were encapsulated.

The XRD patterns as well as the light absorption of perovskite/Cl-GO showed no obvious changes during the test (fig. S20). However, the UV light absorption of perovskite without Cl-GO gradually dropped during the test and the peak of PbI_2 around 500 nm became more prominent, indicating the decomposition of perovskite (fig. S20). The XRD results confirmed decomposition because the signal at 11.8° represents the arising δ phase and the signal at 12.8° could be denoted as emerging PbI_2. The contact angle with water in air rose from 50° for the perovskite sample to 76° for the perovskite/Cl-GO sample (fig. S21). This larger contact angle should enhance moisture stability, as confirmed by UV-vis absorption spectroscopy (fig. S22).

We fabricated PSCs with a perovskite/Cl-GO heterostructure on an aperture area of 1.02 cm^2. The cross-sectional SEM image is shown in Fig. 4A, and the energy levels of the cell are aligned in fig. S23. The current-voltage (*I-V*) curves of cells with different heterostructures are presented in Fig. 4B. The cell with perovskite/Cl-GO obtained a high efficiency of 21.08% under forward scan with a short-circuit current density of 23.82 mA cm^{-2}, an open-circuit voltage of 1.12 V, and a fill factor of 0.79. The detailed parameters for the other two cells can be found in table S2.

Figure 4C shows the incident photo-to-electron conversion efficiency (IPCE) of the cell with perovskite/Cl-GO; the integrated short-circuit current was calculated to be 23.29 mA cm^{-2}, which matched well with the observed short-circuit current. Twenty cells of each batch were fabricated, and the histogram of average power conversion efficiency values is presented in Fig. 4D. The cells with different heterostructures were encapsulated and aged under continuous light-soaking at the maximum power point at 60°C. The corresponding stability results are shown in Fig. 4E; the cell with the heterostructure of perovskite/Cl-GO maintained 90% of its initial value after 1000 hours, whereas the control cell and the cell with GO experienced reductions of 65 and 50%, respectively. The steady-state efficiencies across five cells with perovskite/Cl-GO were tracking at the maximum power point before and after the 1000-hour aging test (fig. S24); no obvious change in steady-state efficiency was found for either fresh or aged cells.

We also sent our aged cell with the perovskite/Cl-GO heterostructure to AIST; a certified stabilized efficiency of 18.6% was obtained on an aperture area of 1.02 cm^2 (fig. S25), which indicates that the device can operate with high efficiency for longer than 1000 hours. In addition, the Spiro-MeOTAD cells exhibited similar performance trends before and after the same aging test, indicating the effectiveness of this stable heterostructure (fig. S26).

We further calculated the ideality factors of the cells with perovskite/PTAA, perovskite/GO/PTAA, or perovskite/Cl-GO/PTAA. The photovoltaic parameters under different light intensity were first measured for each cell (fig. S27); the fresh cells for all three samples showed similar initial ideality factors ranging from 1.35 to 1.51. However, after the aging test, the ideality factor of the cell with perovskite/PTAA or perovskite/GO/PTAA increased to >2 (Fig. 4F), which indicates a serious charge-carrier recombination (*17*, *27*). The cell with the perovskite/Cl-GO heterostructure maintained an ideality factor ~1.6, indicating suppressed interface recombination and efficient charge transfer.

Compared with the perovskite/PTAA and perovskite/GO/PTAA samples, the perovskite/Cl-GO/PTAA sample exhibited the lowest steady-state photoluminescence (PL) signal (fig. S28A), consistent with time-resolved photoluminescence (TRPL) results (fig. S28B). The perovskite film itself had a decay time of 243 ns, but the lifetime in a perovskite/Cl-GO/PTAA heterostructure was 4.1 ns, compared with 5.3 ns in perovskite/GO/PTAA and 5.4 ns in perovskite/PTAA. The charge extraction was also characterized by transient photocurrent decay and photovoltage decay (fig. S28, C and D) (*28*, *29*). The photovoltage decay increased from 22.9 μs (control) to 23.7 μs (GO) and 60.4 μs (Cl-GO), and the photocurrent decay decreased from 1.87 μs (control) to 1.64 μs (GO)

and 1.25 μs (Cl-GO), respectively. These results indicated that reduced charge recombination and more-efficient charge extraction occurred in the perovskite/Cl-GO/PTAA heterostructure.

REFERENCES AND NOTES

1. A. Kojima, K. Teshima, Y. Shirai, T. Miyasaka, *J. Am. Chem. Soc.* **131**, 6050–6051 (2009).
2. J. H. Im, C. R. Lee, J. W. Lee, S. W. Park, N. G. Park, *Nanoscale* **3**, 4088–4093 (2011).
3. H. S. Kim *et al*., *Sci. Rep.* **2**, 591 (2012).
4. M. M. Lee, J. Teuscher, T. Miyasaka, T. N. Murakami, H. J. Snaith, *Science* **338**, 643–647 (2012).
5. E. Edri *et al*., *Nat. Commun.* **5**, 3461 (2014).
6. V. Roiati *et al*., *Energy Environ. Sci.* **7**, 1889–1894 (2014).
7. J. Y. Jeng *et al*., *Adv. Mater.* **25**, 3727–3732 (2013).
8. Y. Wu *et al*., *Nat. Energy* **1**, 16148 (2016).
9. Q. Jiang *et al*., *Nat. Photonics* **13**, 460–466 (2019).
10. A. Amat *et al*., *Nano Lett.* **14**, 3608–3616 (2014).
11. C. Motta *et al*., *Nat. Commun.* **6**, 7026 (2015).
12. F. El-Mellouhi *et al*., *ChemSusChem* **9**, 2648–2655 (2016).
13. S. Kim *et al*., *Sci. Rep.* **7**, 1200 (2017).
14. Y. C. Zhao *et al*., *J. Phys. Chem. C* **121**, 14517–14523 (2017).
15. H. F. Zarick, N. Soetan, W. R. Erwin, R. Bardhan, *J. Mater. Chem. A* **6**, 5507–5537 (2018).
16. G. Y. Kim *et al*., *Nat. Mater.* **17**, 445–449 (2018).
17. W. Tress *et al*., *Energy Environ. Sci.* **11**, 151–165 (2018).
18. G. Beamson, D. Briggs, *High Resolution XPS of Organic Polymers: The Scienta ESCA 300 Database* (Wiley, 1992).
19. R. J. Davis *et al*., *J. Mater. Chem.* **21**, 1721–1729 (2011).
20. D. Konios *et al*., *J. Mater. Chem. A* **4**, 1612–1623 (2016).
21. W. Z. Li *et al*., *J. Mater. Chem. A* **2**, 20105–20111 (2014).
22. H. Zhao *et al*., *Nanotechnology* **27**, 495405 (2016).
23. H. C. Hsu *et al*., *Nanoscale* **5**, 262–268 (2013).
24. D. Luo *et al*., *Science* **360**, 1442–1446 (2018).
25. Z. Hawash, L. K. Ono, S. R. Raga, M. V. Lee, Y. B. Qi, *Chem. Mater.* **27**, 562–569 (2015).
26. J. Luo *et al*., *Energy Environ. Sci.* **11**, 2035–2045 (2018).
27. M. Cai *et al*., *Joule* **2**, 296–306 (2018).
28. Y. Li *et al*., *J. Am. Chem. Soc.* **137**, 15540–15547 (2015).
29. B. Chen, M. Yang, S. Priya, K. Zhu, *J. Phys. Chem. Lett.* **7**, 905–917 (2016).

ACKNOWLEDGMENTS

We thank H. Li and J. Liu from the Instrumental Analysis Center of Shanghai Jiao Tong University (China) for assistance with AFM and KPFM measurements, Z. Bao from the Instrumental Analysis Center of Shanghai Jiao Tong University (China) for assistance with SEM measurements, Y. Han and Y. Zhang from the Instrumental Analysis Center of Shanghai Jiao Tong University (China) for assistance with TOF-SIMS measurements, and Y. Wu from East China University of Science and Technology (China) for assistance with PL and TRPL measurements. **Funding:** This work was supported by the National Natural Science Foundation of China (grant nos. 11574199, 11674219, and 11834011), the Program for Professor of Special Appointment (Eastern Scholar) at Shanghai Institutions of Higher Learning, and a KAKEHI Grant of Japan (grant no. 18H02078). **Author contributions:** Y.W., X.Y., and L.H. conceived of the work. Y.W. and W.K. fabricated and characterized solar cells. Y.W. conducted the SEM, AFM, KPFM, UPS, TOF-SMIS, XRD, UV-vis, PL, and TRPL measurements. T.W. synthesized the GO and Cl-GO and performed the XPS measurements. J.B. conducted the DFT calculation and participated in the discussion of KPFM. D.C. participated in the discussion of UPS results. H.C. assisted with measurement of transient photocurrent and transient photovoltage. Y.W. wrote the first draft of the manuscript. Y.W., X.Y., and L.H. revised the manuscript. All authors analyzed the data and reviewed the manuscript. **Competing interests:** None declared. **Data and materials availability:** All data needed to evaluate the conclusions in the paper are present in the manuscript or the supplementary materials.

SUPPLEMENTARY MATERIALS

science.sciencemag.org/content/365/6454/687/suppl/DC1
Materials and Methods
Supplementary Text
Figs. S1 to S28
Tables S1 and S2
References (*30*–*36*)

25 April 2019; accepted 17 July 2019
10.1126/science.aax8018

Science

Stabilizing heterostructures of soft perovskite semiconductors

Yanbo Wang, Tianhao Wu, Julien Barbaud, Weiyu Kong, Danyu Cui, Han Chen, Xudong Yang and Liyuan Han

Science **365** (6454), 687-691.
DOI: 10.1126/science.aax8018

Strong perovskite interfaces

The weak bonding in the crystal lattice of hybrid perovskites used in solar cells promotes surface decomposition and interferes with the formation of stable heterostructures with the charge carrier layers. Y. Wang *et al.* show that strong bonds are formed between lead and both chlorine and oxygen atoms in a film with a lead-rich surface and a chlorinated graphene oxide layer. This interface was used with common hole-transporting materials to fabricate solar cells that maintained 90% of their initial efficiency of 21% after operation at 60°C for 1000 hours.

Science, this issue p. 687